

# A flamelet model with heat-loss effects for predicting wall-heat transfer in rocket engines

Peter C. Ma\*, Hao Wu\* and Matthias Ihme<sup>†</sup>

*Stanford University, Stanford, CA 94305*

Jean-Pierre Hickey<sup>‡</sup>

*University of Waterloo, Waterloo, ON N2L 3G1, Canada*

**A flamelet-based combustion model is proposed for the prediction of wall-heat transfer in rocket engines and confined combustion systems. To account for the impact of the flame due to convective heat loss on the wall, a permeable thermal boundary condition is introduced in the counter-flow diffusion flame configuration. The solution of the resulting non-adiabatic flame structure forms a three-dimensional manifold, which is parameterized in terms of mixture fraction, progress variable, and temperature. The performance of the model is first evaluated through a DNS analysis of a  $H_2/O_2$  diffusion flame that is stabilized at an inert isothermal wall. The developed non-adiabatic flamelet model is shown to accurately predict the temperature, chemical composition, and wall heat transfer. Combined with a presumed PDF-closure, the model is then applied to LES of a single-injector rocket combustor to examine effects of heat-transfer on the turbulent flame structure in rocket engines.**

## I. Introduction

Turbulent combustion processes in technical systems, such as furnaces, internal combustion engines, gas turbines, and rocket motors require the consideration of heat transfer and flame-wall interactions.<sup>1</sup> In particular, a major source for failures in the early design of rocket engines is attributed to the inadequate characterization of heat transfer to the injector face plate, the combustion chamber, and the rocket skirt.<sup>2,3</sup> Therefore, the capability of accurately predicting the thermal loading is crucial for reducing uncertainties during the early development of rocket engines. The convective heat transfer rate from the hot gas to the solid surface is essential to the cooling of the combustion and thrust chamber walls, which has a direct impact on their life time.<sup>4</sup>

Several challenges arise in the modeling of turbulent combustion processes that are characterized by significant heat-losses. In particular, strong heat-losses can lead to flame-quenching, enhanced emissions, and combustion instabilities.<sup>5–12</sup> Another issue is that the heat flux introduces a dependence on the alignment between flame and wall, spanning the limiting cases of head-on quenching and side-wall quenching.<sup>1</sup> Finally, the description of the thermo-viscous boundary layer structure introduces substantial resolution requirements, and wall-modeled LES for the accurate prediction of wall heat transfer is still an ongoing research topic.<sup>13–16</sup>

Despite the remarkable progress in the development of computational methods for the prediction of rocket motors, the issue of modeling heat-transfer has only recently found some attention. Most notable is the coordinated effort by Tucker et al.<sup>17</sup> on assessing current modeling capabilities in predicting wall-heat transfer in a uni-element rocket injector. Although various modeling approaches (LES, U/RANS), combustion models (finite-rate chemistry, flamelet formulations), algorithms, and grid arrangements (two and three-dimensional computational domains), as well as different turbulence and subgrid-closure models

---

\*Graduate Research Assistant, Department of Mechanical Engineering.

<sup>†</sup>Assistant Professor, Department of Mechanical Engineering.

<sup>‡</sup>Assistant Professor, Department of Mechanical and Mechatronics Engineering.

were employed, the outcome of this work represents an important step in establishing a benchmark for assessing the predictive capability of currently employed rocket-engine modeling tools.

The objective of this work is to develop a flamelet-based combustion model for the prediction of wall-heat transfer in rocket engines. Commonly employed flamelet models that are based on steady flamelet formulations rely on the underlying assumption that the flame state of a particular flamelet relaxes to the steady-state solution on a sufficiently fast time scale.<sup>18–21</sup> However, heat-loss processes that are associated with radiative and convective heat transfer evolve on time scales that are slow compared to chemical processes in typical combustion applications. To incorporate these non-adiabatic processes into the steady-state flamelet formulation, extensions have been proposed.<sup>22–30</sup> These extensions considered the modeling of radiative and convective heat losses, which were achieved by introducing enthalpy defect variables, including sink terms in the energy equation, or by rescaling the heat-release rate. While these models provided improved predictions for temperature, they introduce assumptions about excess enthalpy, locality of the heat-loss, and boundary conditions that limit their extension to turbulent diffusion flames.

The present work considers the modeling of wall-heat transfer in the context of diffusion flames. To this end, convective heat-loss effects are introduced into the flamelet formulation locally to represent sidewall quenching in a physically consistent representation. The mathematical model is described in the next section. The accuracy of this non-adiabatic flamelet model is examined through DNS in Section IV. The model is subsequently applied in LES of a uni-element rocket injector in Section V. The paper finishes with conclusions.

## II. Governing equations

The governing equations are the Favre-averaged conservation equations for mass, momentum, total energy, mixture fraction, mixture fraction variance, and progress variable, written as follows:

$$\frac{\partial \bar{\rho}}{\partial t} + \frac{\partial \bar{\rho} \tilde{u}_j}{\partial x_j} = 0, \quad (1a)$$

$$\frac{\partial \bar{\rho} \tilde{u}_i}{\partial t} + \frac{\partial \bar{\rho} \tilde{u}_i \tilde{u}_j}{\partial x_j} = -\frac{\partial \bar{p}}{\partial x_i} + \frac{\partial}{\partial x_j} \left[ (\tilde{\mu} + \mu_t) \left( \frac{\partial \tilde{u}_i}{\partial x_j} + \frac{\partial \tilde{u}_j}{\partial x_i} - \frac{2}{3} \delta_{ij} \frac{\partial \tilde{u}_k}{\partial x_k} \right) \right], \quad (1b)$$

$$\begin{aligned} \frac{\partial \bar{\rho} \tilde{E}}{\partial t} + \frac{\partial \bar{\rho} \tilde{u}_j \tilde{E}}{\partial x_j} &= \frac{\partial}{\partial x_j} \left[ \left( \frac{\tilde{\lambda}}{c_p} + \frac{\mu_t}{\text{Pr}_t} \right) \frac{\partial \tilde{h}}{\partial x_j} - \tilde{u}_j \bar{p} + \tilde{u}_i (\bar{\tau}_{ij} + \bar{\tau}_{ij}^R) \right] \\ &+ \frac{\partial}{\partial x_j} \left[ \sum_{k=1}^N \left( \bar{\rho} \tilde{D}_k - \frac{\tilde{\lambda}}{c_p} \right) \tilde{h}_k \frac{\partial \tilde{Y}_k}{\partial x_j} \right], \end{aligned} \quad (1c)$$

$$\frac{\partial \bar{\rho} \tilde{Z}}{\partial t} + \frac{\partial \bar{\rho} \tilde{u}_j \tilde{Z}}{\partial x_j} = \frac{\partial}{\partial x_j} \left[ \left( \bar{\rho} \tilde{D} + \frac{\mu_t}{\text{Sc}_t} \right) \frac{\partial \tilde{Z}}{\partial x_j} \right], \quad (1d)$$

$$\frac{\partial \bar{\rho} \tilde{Z}''^2}{\partial t} + \frac{\partial \bar{\rho} \tilde{u}_j \tilde{Z}''^2}{\partial x_j} = \frac{\partial}{\partial x_j} \left[ \left( \bar{\rho} \tilde{D} + \frac{\mu_t}{\text{Sc}_t} \right) \frac{\partial \tilde{Z}''^2}{\partial x_j} \right] + 2 \frac{\mu_t}{\text{Sc}_t} \frac{\partial \tilde{Z}}{\partial x_j} \frac{\partial \tilde{Z}}{\partial x_j} - \bar{\rho} \tilde{\chi}, \quad (1e)$$

$$\frac{\partial \bar{\rho} \tilde{C}}{\partial t} + \frac{\partial \bar{\rho} \tilde{u}_j \tilde{C}}{\partial x_j} = \frac{\partial}{\partial x_j} \left[ \left( \bar{\rho} \tilde{D} + \frac{\mu_t}{\text{Sc}_t} \right) \frac{\partial \tilde{C}}{\partial x_j} \right] + \bar{\omega}_C, \quad (1f)$$

where  $u_i$  is the  $i$ th component of the velocity vector,  $E$  is the total energy including the chemical energy,  $C$  is the progress variable,  $\mu$  and  $\mu_t$  are the laminar and turbulent viscosity,  $\lambda$  is the thermal conductivity,  $D$  is the diffusion coefficient for the scalars,  $\bar{\omega}_C$  is the source term for the progress variable,  $\tau_{ij}$  and  $\tau_{ij}^R$  are the viscous and subgrid-scale stresses which are assumed to take the form as the second term on the right-hand side of Eq. (1b),  $\text{Pr}_t$  is the turbulent Prandtl number, and  $\text{Sc}_t$  is the turbulent Schmidt number. An appropriate subgrid-scale model is needed for the computation of the turbulent viscosity  $\mu_t$ . Under the unity Lewis number assumption, the summation on the right-hand side of Eq. (1c) vanishes so that the species mass fractions are not explicitly required for the energy equation. The system is closed with the flamelet-based combustion model that will be discussed in the next section. The ideal-gas equation of state  $\bar{p} = \bar{\rho} \tilde{R} \tilde{T}$  is used for the computation of pressure.

The massively paralleled, finite-volume solver, CharLES<sup>x</sup>, developed at the Center for Turbulence Research is used in this study. A control-volume based finite-volume approach is utilized for the discretization

of the system of equations, Eq. (1):

$$\frac{\partial \mathbf{U}}{\partial t} V_{cv} + \sum_f \mathbf{F}^e A_f = \sum_f \mathbf{F}^v A_f + \mathbf{S} V_{cv}, \quad (2)$$

where  $\mathbf{U}$  is the vector of conserved variables,  $\mathbf{F}^e$  is the face-normal Euler flux vector,  $\mathbf{F}^v$  is the face-normal viscous flux vector which corresponds to the r.h.s of Eq. (1),  $\mathbf{S}$  is the source term vector,  $V_{cv}$  is the volume of the control volume, and  $A_f$  is the face area. A strong stability preserving 3rd-order Runge-Kutta (SSP-RK3) scheme<sup>31</sup> is used for time advancement.

The convective flux is discretized using a sensor-based hybrid scheme in which a high-order, non-dissipative scheme is combined with a low-order, dissipative scheme to minimize the numerical dissipation introduced.<sup>32</sup> A central scheme which is fourth-order on uniform meshes is used along with a second-order ENO scheme for the hybrid scheme and a density sensor<sup>33,34</sup> is adopted in this study. An entropy-stable flux correction technique<sup>34</sup> is used to ensure the physical realizability of the numerical solutions including the positivity of scalars and to dampen the non-linear instabilities in the numerical solutions.

### III. Combustion Model

The present work is concerned with the modeling of wall-heat loss effects and flame/wall interaction in the context of the laminar flamelet formulation.<sup>35</sup> In this formulation, the direction of heat flux is assumed to be primarily aligned with the gradient of mixture fraction, i.e. normal to the flame surface. As a result, heat losses can be introduced by an additional thermal boundary condition, whose location in mixture-fraction coordinate is denoted by  $Z_{\text{wall}}$ . This is illustrated in Fig. 1, showing the schematic of the counterflow diffusion flame.

This configuration is modified by introducing an isothermal and chemically inert wall. Without loss of generality, we assume in this study that the wall approaches the flame from the fuel-rich side. This wall is permeable and corresponding boundary conditions in physical space are:

$$x = x_{\text{wall}} : T = T_{\text{wall}}; \partial_x \mathbf{Y}|_{x_{\text{wall}}^+} = \partial_x \mathbf{Y}|_{x_{\text{wall}}^-}; \partial_x Z = 0, \quad (3)$$

where  $x_{\text{wall}}$  identifies the wall location and the superscripts  $+/-$  denote the two sides of the wall. The last condition ensures continuity of species flux, and  $\partial_x$  denotes the partial derivative with respect to the axial coordinate  $x$ . In this context, it is noted that this model can be extended by considering more

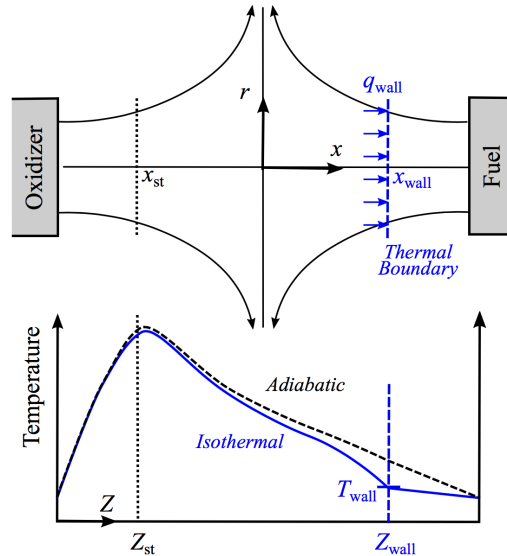


Figure 1. Schematic of counter-flow diffusion flame corresponding flame-normal heat transfer in which the heat-flux vector is aligned with the mixture-fraction gradient.

general boundary conditions, for instance by including surface-catalytic effects, heat-flux conditions, or wall-recombination reactions. After applying the flamelet transformation to the conservation equations for species and energy under consideration of boundary conditions give in Eq. (3), the non-adiabatic flamelet equations take the following form:

$$\partial_t \mathbf{Y} - \frac{\chi_Z}{2} \frac{\partial^2 \mathbf{Y}}{\partial Z^2} = \dot{\omega}, \quad (4a)$$

$$\partial_t T - \frac{\chi_Z}{2} \frac{\partial^2 T}{\partial Z^2} - \frac{\chi_Z}{2} \frac{\partial \ln(c_p)}{\partial Z} \frac{\partial T}{\partial Z} = \frac{\dot{q}_H}{c_p}, \quad (4b)$$

for  $Z \in (0, Z_{\text{wall}})$ , and

$$\partial_t \mathbf{Y} - \frac{\chi_Z}{2} \frac{\partial^2 \mathbf{Y}}{\partial Z^2} = \mathbf{0}, \quad (5a)$$

$$\partial_t T - \frac{\chi_Z}{2} \frac{\partial^2 T}{\partial Z^2} - \frac{\chi_Z}{2} \frac{\partial \ln(c_p)}{\partial Z} \frac{\partial T}{\partial Z} = 0, \quad (5b)$$

for  $Z \in (Z_{\text{wall}}, 1)$ . These equations are solved subject to the boundary conditions:

$$Z = 0: \quad T = T_O; \quad \mathbf{Y} = \mathbf{Y}_O, \quad (6a)$$

$$Z = Z_{\text{wall}}: \quad T = T_{\text{wall}}; \quad \mathbf{Y}|_{Z_{\text{wall}}^-} = \mathbf{Y}|_{Z_{\text{wall}}^+}; \quad \partial_Z \mathbf{Y}|_{Z_{\text{wall}}^-} = \partial_Z \mathbf{Y}|_{Z_{\text{wall}}^+}, \quad (6b)$$

$$Z = 1: \quad T = T_F; \quad \mathbf{Y} = \mathbf{Y}_F, \quad (6c)$$

where  $Z_{\text{wall}}$  is a model parameter representing the location of the thermal boundary condition transformed into the mixture-fraction coordinate. The subscripts ‘‘F’’ and ‘‘O’’ refer to conditions in the fuel and oxidizer stream, respectively. Although Eqs. (4) and (5) are written for unity Lewis-number flames, this model can be directly extended to account for preferential diffusion. Due to the Neumann boundary condition of the mixture fraction at the wall, the scalar dissipation rate is thus modified to be:

$$\chi_Z = \chi_{\text{st}} \exp \left\{ -2 \left( \text{erfc}^{-1}(2Z/Z_{\text{wall}}) \right)^2 + 2 \left( \text{erfc}^{-1}(2Z_{\text{st}}/Z_{\text{wall}}) \right)^2 \right\}. \quad (7)$$

The location and the temperature of the wall condition can be modified to span the entire gamut of possible conditions. The specification of the wall-conditions can also be acquired through measurements of mixture fraction and temperature in the near wall region. Thermal quenching will occur as the wall approaches the flame and the heat loss is amplified.

The non-adiabatic flamelet model proposed contains three different time scales, representing the characteristic diffusion time scale  $\tau_{\text{diff}}$ , the convective heat-transfer time scale  $\tau_{\text{conv}}$ , and the characteristic chemical time scale  $\tau_{\text{chem}}$ . The convective time scale is not explicitly specified but embedded in the time scale for the change of  $Z_{\text{wall}}$ . The ratio between these scales can be written as:<sup>36,37</sup>

$$\tau_{\text{diff}} : \tau_{\text{conv}} : \tau_{\text{chem}} = \text{Da} : \frac{\text{DaPr}}{\text{Nu}_L} \frac{L^2}{\delta_f^2} : 1, \quad (8)$$

where Da is the Damköhler number, Pr is the Prandtl number,  $\text{Nu}_L$  is the Nusselt number associated with the device length scale  $L$ , and  $\delta_f$  is the characteristic flame length scale. For combustion in rocket engines, the first two terms on the right-hand-side are both much greater than unity, indicating that the species distribution of the flamelet is able to directly respond to temperature variations by heat-loss effects, since the characteristic chemical time is short compared to the time scales associated with diffusion and convection. It is thus justified to solve Eqs. (4) and (5) under steady-state conditions.

The flamelet calculations are performed using a modified FLAMEMASTER solver.<sup>38</sup> Sample solutions at the condition specified in Section V are shown in Fig. 2. The results are obtained at  $\chi_{\text{st}} = 200s^{-1}$  with  $Z_{\text{wall}}$  approaching the flame from the fuel side. The monotonic decrease of temperature shows an increasing level of heat loss as  $Z_{\text{wall}}$  approaches  $Z_{\text{st}}$ . Despite the fact that the maximum flame temperature decreases by 2000 K, the mass fraction of the product species  $\text{H}_2\text{O}$  shows much less sensitivity and is almost unaffected by the heat loss beyond the reactive region. On the other hand, the hydroxyl-radical mass fraction is significantly reduced. This observation suggests that the difference between the mass fraction of OH and  $\text{H}_2\text{O}$  may serve as a diagnostic for the presence of convective heat losses to the wall.

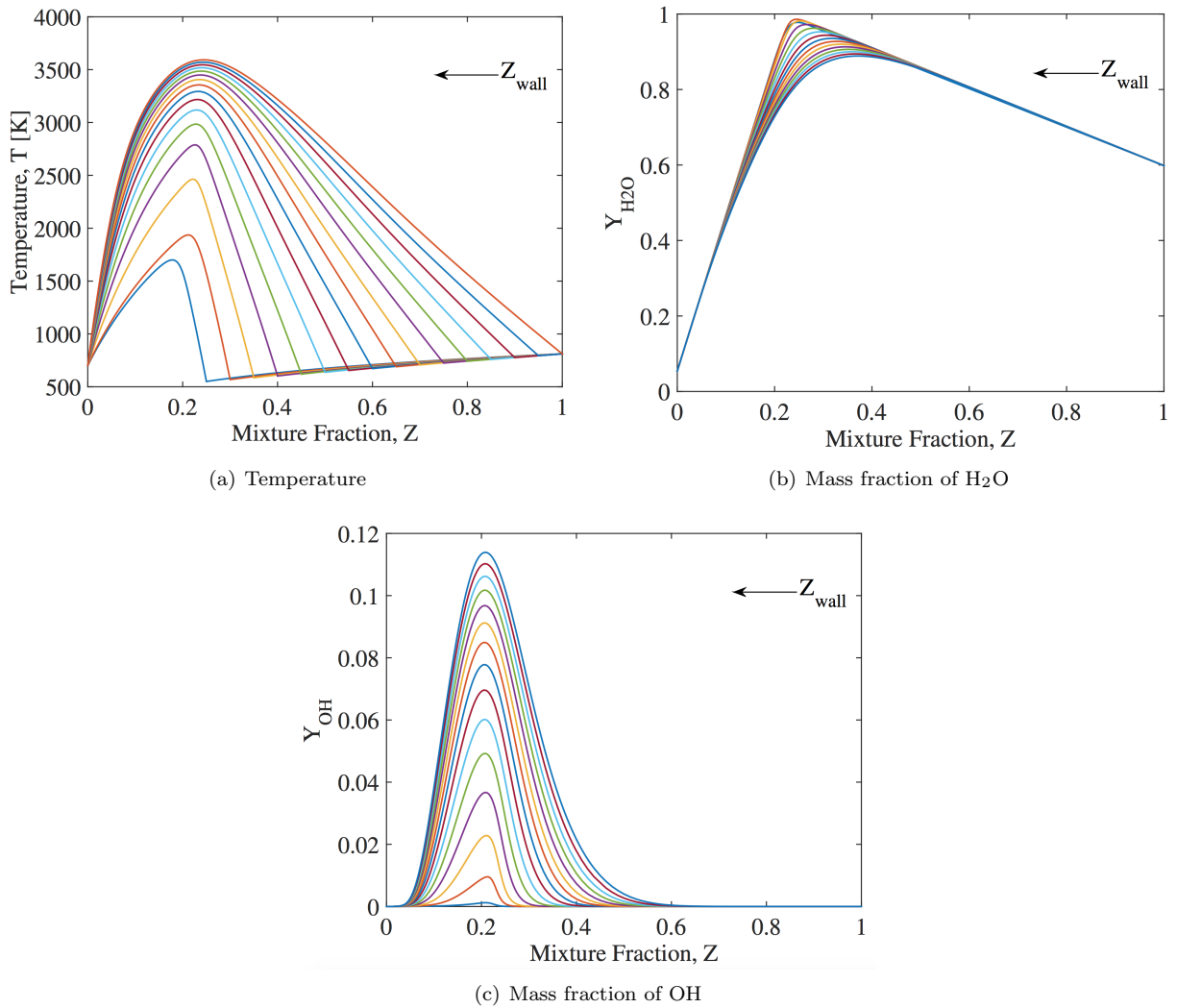


**Figure 2.** FPV-WHT solution of (a) temperature, (b) mass fraction of  $\text{H}_2\text{O}$ , and (c) mass fraction of  $\text{OH}$  with respect to different  $Z_{\text{wall}}$  at  $\chi_{\text{st}} = 200\text{s}^{-1}$ . Maximum flame temperature and  $\text{OH}$  mass fraction decrease with increasing heat loss effects.

For a user-specified wall temperature, the steady-state solutions to Eqs. (4) and (5) are obtained with respect to a variation in  $\chi_Z$  and  $Z_{\text{wall}}$ , which generates a three-dimensional manifold. This manifold is subsequently parameterized by mixture fraction, progress variable, and temperature:  $\psi = \mathcal{F}_\psi(Z, C, T)$ , where  $\psi$  represents the vector of thermo-physico-chemical quantities. In this context it is noted that the total enthalpy is commonly used for the parameterization of non-adiabatic system. However, for the case of flame quenching and variations in temperature-boundary conditions, the enthalpy is a non-monotonic function. In contrast, as shown in Fig. 2(a), temperature provides a unique representation of the flame-structure in the presence of wall heat losses. We will refer to this model as flamelet/progress variable model with wall-heat transfer (FPV-WHT). For comparison purposes, the flamelet/progress variable model developed by Saghafian et al.<sup>39</sup> for compressible flows will also be examined. In this model, the specific heat ratio is modeled as a linear function of temperature in order to primitive variables from conservative variables. Details can be found in Saghafian et al.<sup>39</sup> and this model is referred to as model FPV-LIN.

In the following, we will examine the performance of FPV-WHT model by considering a DNS-configuration to examine the validity of essential modeling assumptions. This model is subsequently applied in an large-eddy simulation of a uni-element rocket injector that was experimentally investigated by Pal et al.<sup>40</sup>

## IV. DNS Analysis of FPV-WHT Model

### A. DNS configuration

A DNS is performed to examine the effect of the conductive wall-heat flux on the flame structure and to evaluate the performance of the model. The simulation is conducted using a low-Mach solver and details about the numerical solver and governing equations solved can be found in Wu and Ihme.<sup>41</sup> This DNS-configuration considers the stabilization of a hydrogen/oxygen flame near a planar wall, and follows the configuration studied by Wang and Trouvé.<sup>42</sup> The simulation is conducted in a three-dimensional, spanwise-periodic domain with an inflow boundary condition specified at  $x/\delta = 0$ , a wall boundary at  $y/\delta = 0$ , and convective outflow boundaries at  $x/\delta = 15$  and  $y/\delta = 6$ . The temperature condition at the slip-free wall is either specified by a constant temperature of 300 K (non-adiabatic) or homogeneous Neumann condition (adiabatic). The velocity inflow profile is prescribed by a synthetic turbulent flow, of which the mean flow obeys the law of the wall<sup>43</sup> with boundary-layer thickness of  $\delta = 1$  cm. The turbulent perturbations with turbulence intensity of 0.2 in the freestream are generated using the method of Klein et al.<sup>44</sup> The mesh in wall-normal distance is discretized using 320 grid points following an exponential growth rate, and ten grid-points are used to resolve the viscous sublayer. The mesh in streamwise and spanwise directions is uniform using 400 and 64 points, respectively.

The non-premixed combustion is over-ventilated with the fuel injected through a slit of height  $\delta$  above the wall. While the non-adiabatic FPV-model is equipped with the capability to account for detailed reaction chemistry, the present DNS study considers a single-step reaction to focus on convective heat-loss effects to the wall. The rate-coefficients for this  $\text{H}_2/\text{O}_2$ -system are taken from Marinov et al.<sup>45</sup> The consideration of detailed chemistry and complex transport properties is addressed in Sec. V. Relevant to preburner conditions, the fuel composition is  $Y_{\text{H}_2} = 0.2$  and  $Y_{\text{H}_2\text{O}} = 0.8$ , and the composition in the oxidizer stream is  $Y_{\text{O}_2} = 0.6$  and  $Y_{\text{H}_2\text{O}} = 0.4$ . The temperature in both streams is set to 300 K and the pressure is 1 bar. Further model assumptions employed in this DNS include constant specific heat, temperature-dependent dynamic viscosity, a constant Prandtl number of  $\text{Pr} = 0.7$ , the ideal-gas equation of state, and unity Lewis numbers. The impact of these assumptions and choices are discussed by Wang and Trouvé.<sup>42</sup>

### B. Model analysis

In this section, we evaluate the accuracy of the FPV-WHT model through direct comparisons against DNS-data. The DNS solves transport equations for species mass fractions and temperature, for which the source terms are directly evaluated. In contrast, the FPV-WHT model retrieves all thermochemical quantities from a flamelet table  $\mathcal{F}_\psi(Z, C, T)$ , which requires the solution of conservations equations for mixture fraction, progress variable, and temperature. The chemistry table is generated from the solution of the flamelet (Eqs. (4) and (5)) by varying the wall-boundary location between  $Z_{\text{st}} \leq Z_{\text{wall}} \leq 1$ . All simulations are spatially resolved so that no turbulence closure is employed. To examine the importance of heat-loss effects on the flame, an additional FPV-WHT calculation is performed in which the wall is described by adiabatic boundary conditions. All simulations are performed on the same mesh and using the same boundary conditions.

Comparison of the instantaneous temperature fields for these three simulations are presented in Fig. 3. To facilitate a direct comparisons, results are shown at the same time instance. In this figure, the solid black line represents the location of stoichiometric mixture. This direct comparison shows good qualitative agreement between DNS and the FPV-WHT calculation. Clearly visible is the thermal boundary layer, and the onset of thermal quenching at  $x/\delta \approx 8.5$ . The high turbulence level of the inlet stream leads to the formation of unburned fuel pockets that burn out as they are advected downstream. Results from the FPV-WHT calculation with adiabatic wall (bottom panel of Fig. 3) provide a direct assessment of convective heat-loss effects on the flame. Specifically, substantial flame/wall interactions are observed for  $x/\delta \geq 5$ . Associated with a lower temperature in the boundary layer due to the heat transfer is the reduction of dilation. This results in a smaller boundary layer, thereby pushing the flame closer to the wall.

Quantitative comparisons of simulation results are presented in Fig. 4, showing wall-normal profiles of mean temperature (left) and mean water mass fraction (right) at different streamwise locations. For both quantities, the non-adiabatic FPV model provides an accurate predictions compared with the DNS results. Effects of heat-losses are observed to be more significant for temperature than for species. The impact becomes stronger with increasing downstream position and the amount of convective heat-loss accumulates,

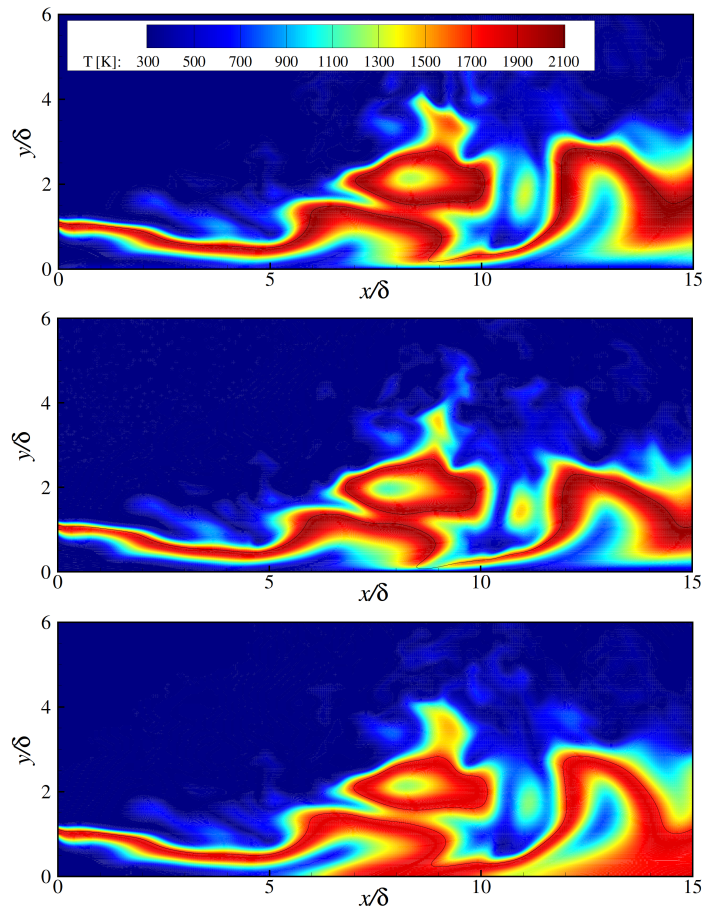


Figure 3. Instantaneous temperature field obtained from (top) DNS, (middle) FPV-WHT with isothermal wall, and (bottom) FPV-WHT with adiabatic wall; solid black lines represent the stoichiometric mixture with  $Z_{st} = 0.273$ .

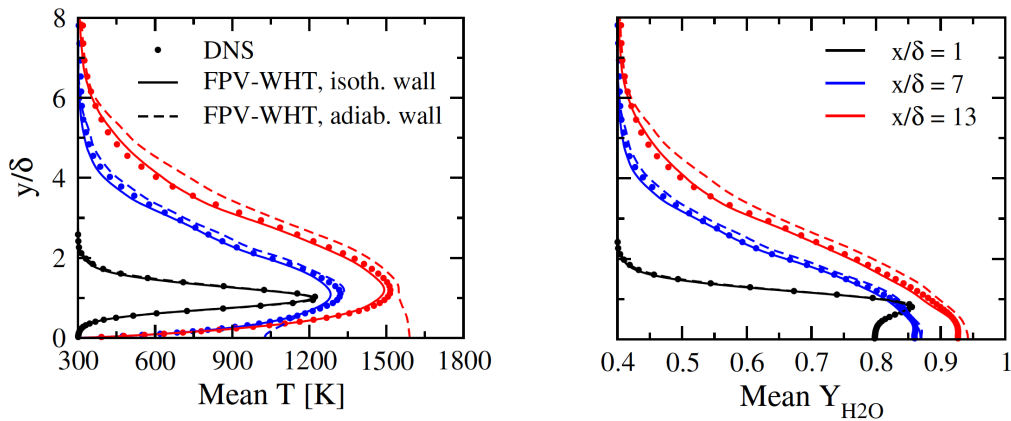


Figure 4. Comparison of mean temperature (left) and mass fraction of  $H_2O$  (right) obtained at different streamwise location between DNS, FPV-WHT with isothermal wall, and FPV-WHT with adiabatic wall.

which is indicated by the larger deviation between both FPV-WHT simulations. In this figure, the importance of thermal wall quenching is apparent for the  $x/\delta = 13$ , where the adiabatic FPV-WHT calculation shows the highest temperature of 1650 K at the wall, while the FPV-WHT calculation with isothermal walls predicts quenching.

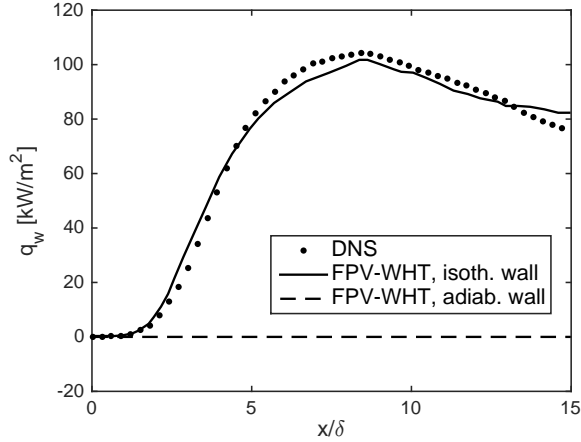


Figure 5. Comparison of heat flux at the wall obtained from DNS and FPV-WHT model.

We also compare the predictions for wall-heat flux between FPV-WHT and DNS. The accurate prediction of the heat-flux is essential for engineering applications. As shown in Fig. 5, the maximum heat flux is about  $110 \text{ kW/m}^2$  and appears at  $x/\delta = 8$ . It is seen that the herein proposed FPV-WHT formulation accurately predicts the heat flux profile along the wall, and deviation with the DNS results is less than 5 percent.

## V. Application to LES of Single-Injector Rocket Combustor

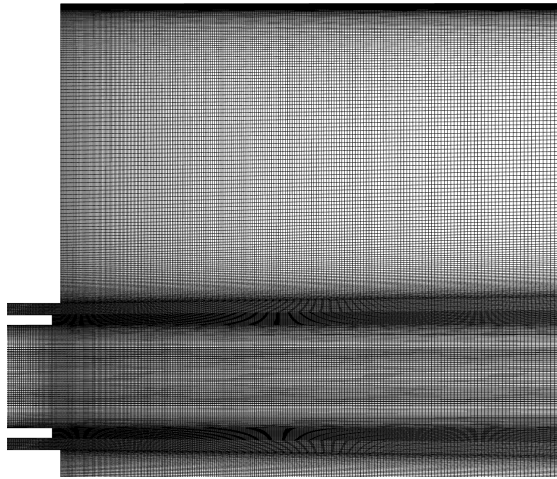
### A. Experimental configuration and computational setup

In this section, the FPV-WHT model is applied in LES of a uni-element rocket injector that was experimentally investigated by Pal et al.<sup>40</sup> The experimental configuration consists of the main rocket chamber having a diameter of 38.1 mm, as shown in Fig. 6(a). Two propellant preburners supply gaseous hydrogen and oxygen to the coaxial injector. The central injector nozzle has a diameter of 5.26 mm ( $\equiv \delta$ ) and supplies the oxidizer having a composition of  $Y_{\text{O}_2} = 0.9458$  and  $Y_{\text{H}_2\text{O}} = 0.0542$  at a temperature of  $T = 700 \text{ K}$ . The fuel is supplied by an annulus surrounding the inner oxidizer stream, having inner and outer diameters of 6.3 mm and 7.49 mm, respectively. The fuel composition is  $Y_{\text{H}_2} = 0.4018$  and  $Y_{\text{H}_2\text{O}} = 0.5982$  and the temperature is  $T = 811 \text{ K}$ . The post, separating the fuel and oxidizer stream, is recessed with respect to the injector end wall, and the recess height was estimated to be 0.43 mm at fired condition. The pressure in the chamber during the steady-state operation was reported to be 54.2 bar. The bulk exit velocities of the injector are 154 m/s for the oxidizer stream and 764 m/s for the fuel stream. The corresponding Reynolds numbers based on the hydraulic diameter are  $6 \times 10^5$  and  $1.7 \times 10^5$ , respectively.

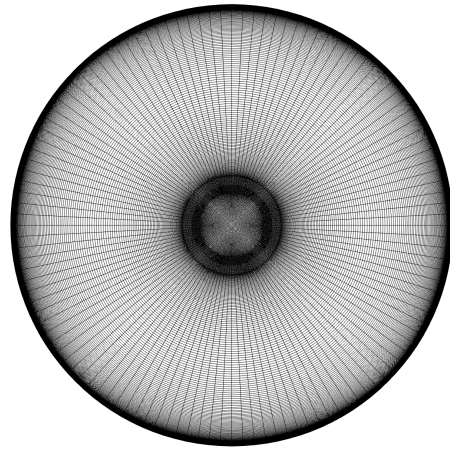
A multi-block structured mesh is used for the discretization of the computational domain, which is shown in Fig. 6. The axial direction is discretized with 600 grid points for the combustion chamber following a linear growth rate, and 250 grid points are used in radial direction. The circumferential direction is equally spaced and uses 120 points. To avoid additional uncertainties associated with the wall modeling, the thermo-viscous boundary layer is fully resolved to capture the heat flux at the wall. The minimum wall spacing along the chamber wall is  $10 \text{ }\mu\text{m}$ , which gives  $y^+ \approx 2$  for most of the cells at the chamber wall. The grid is clustered in the near-injector region with minimum spacing of  $20 \text{ }\mu\text{m}$ , as shown in Figs. 6(b) and 6(c). Mass flow rate and temperature are specified at the inflow boundary conditions. Synthetic turbulence is generated for both inflow streams using the digital filter method.<sup>44</sup> Supersonic outflow boundary condition is specified at the outlet. No-slip conditions are applied at all wall surfaces. Injector wall surfaces are assumed to be adiabatic. The face of the combustion chamber and oxidizer post tip have a temperature at 755 K. The temperature profile along the chamber wall is obtained from experimental measurements as a one-dimensional axial profile<sup>17</sup> and a spline interpolation is used for the intermediate temperature between experimental data. The nozzle temperature is assumed to be fixed at 510 K. A Vreman subgrid-scale model<sup>46</sup> is applied for the closure of the turbulence of velocity field. The  $\text{H}_2/\text{O}_2$ -chemistry was described by the detailed mechanism



(a) Computational domain and overall view of the mesh



(b) Center-plane mesh near injector



(c) Transverse cut of mesh near injector

**Figure 6. Computational domain and mesh.**

due to Burke et al.<sup>47</sup> The turbulence-combustion interaction is modeled using a presumed PDF-closure; a beta-PDF is used for mixture fraction, and distributions for progress variable and temperature are described by Dirac-delta functions. The flow field is initialized with hot products in the chamber and fuel and oxidizer at corresponding temperatures in the two injectors. The initial velocity field is set based on the overall mass flow rate and the density of the hot product. The flow inside the nozzle is initialized with a one-dimensional solution for converging-diverging nozzles. Two flow-through times are used to flush out the initial transient and reach a steady state. The CFL number is set to one during the simulation, which gives a typical time step size of 5 ns during steady state.

Thermocouples were mounted to the chamber wall to measure wall temperature and heat flux in the experiment, and these heat flux measurements were used as comparison in the following. Since a finite-volume solver is utilized, the heat flux which is the boundary flux due to enthalpy gradient for the energy equation from the simulations is taken for the comparison with measurements. No subgrid-scale model is applied at the wall and the heat flux is only due to resolved laminar heat transfer.

## B. Simulation results

To assess effects of wall-heat transfer on the flow-field structure and the performance of the developed models, LES calculations with both the FPV-WHT and FPV-LIN model are conducted. Three cases are considered, the FPV-LIN model with adiabatic wall, the FPV-LIN model with isothermal wall, and the FPV-WHT with isothermal wall. The simulation with adiabatic wall boundary conditions is conducted to evaluate effects of wall heat transfer on the flow field and combustion dynamics. For this case, the FPV-LIN and FPV-WHT

models are expected to yield similar results since no heat loss effects are present. The FPV-LIN model, which utilizes an adiabatic flamelet table without taking into account the heat loss effects, is used as a baseline model for comparison with the FPV-WHT model.

Figure 7 shows the instantaneous results of the temperature field at the center-plane obtained from the three cases conducted to give an overview of the flowfield features. It can be seen from Fig. 7 that near the injector, a diffusion flame separates the hydrogen and oxygen streams. The oxygen core extends downstream for about 50 mm ( $\approx 9.4\delta$ ) until it breaks down. A recirculation zone is present at the corners of the combustor chamber which is induced by the mixing of the hydrogen stream and the hot combustion product. The flow accelerates after the breakdown of the oxygen core due to the recirculation zone and thermal expansion. The chemical equilibrium is almost reached further downstream and the flow can be considered as a axisymmetric pipe flow of the hot combustion product until the converging-diverging nozzle.

Comparing the three temperature fields in Fig. 7, the effects of the heat loss at the wall can clearly be seen. The temperature obtained from both the FPV-LIN and FPV-WHT models with isothermal wall boundary conditions show lower temperatures both in the recirculation zone and the pipe flow region downstream. Adiabatic flame temperature of the hydrogen/oxygen flame is reached in the adiabatic case, which is about 3500 K as can be seen from Fig. 2(a). The decrease of the temperature compared with the adiabatic case is about 300 K and 200 K for the isothermal case with FPV-LIN and FPV-WHT models, respectively. The shape of the diffusion flame is not significantly affected by the presence of the wall heat loss although relatively low temperature flow is convected towards the hydrogen stream from the recirculation bubble. The difference between FPV-LIN and FPV-WHT models show the effects of including heat loss effects on the flame structure. Specifically, slightly higher temperature over the combustor chamber can be observed with the FPV-WHT model.

The simulations are conducted for another flow-through time to obtain statistical results. The simulation results are also averaged in azimuthal direction. Figure 8 shows the mean temperature profiles at the center-plane for the three cases performed in this study. The results are consistent with the instantaneous temperature fields as shown in Fig. 7, and the radial profiles of the mean temperature are plotted in Fig. 9 at several axial locations to better interpret simulation results. As shown in Figs. 8 and 9, the case with adiabatic wall shows significant higher mean temperature near the injector, where the difference can be more than 500 K. With increasing downstream distance the temperature inside the combustor core region equilibrates, and heat-loss effects become increasingly confined to the combustor-wall region. Comparing

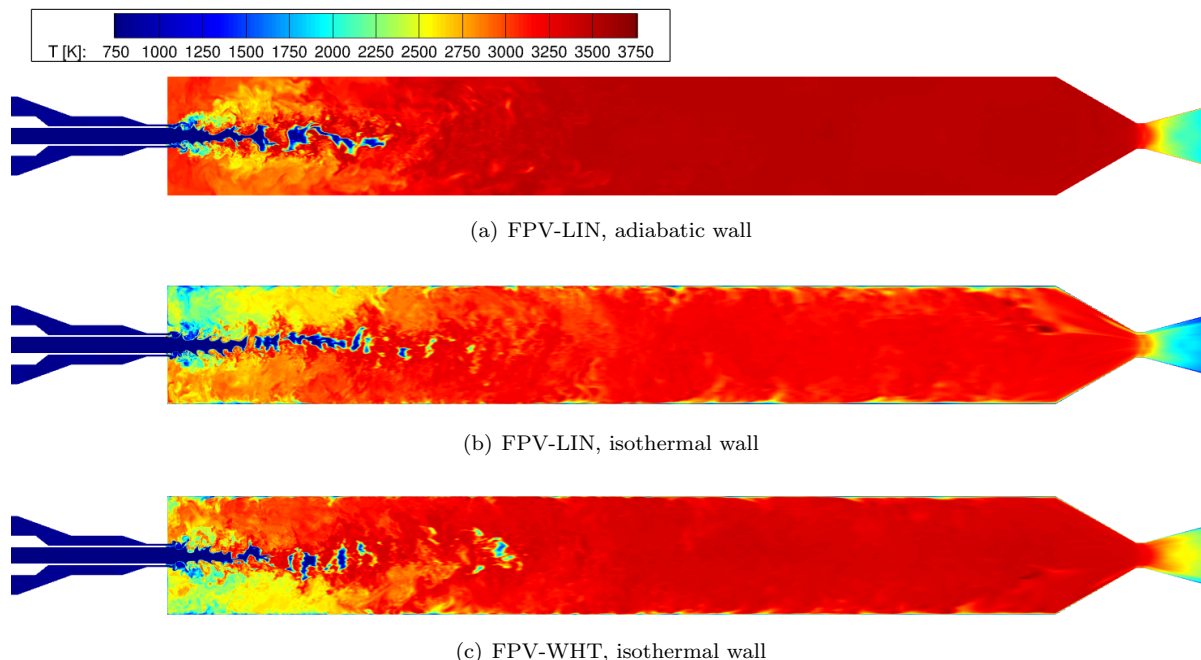


Figure 7. Instantaneous temperature field at the center-plane for (a) FPV-LIN with adiabatic wall, (b) FPV-LIN with isothermal wall, and (c) FPV-WHT with isothermal wall.

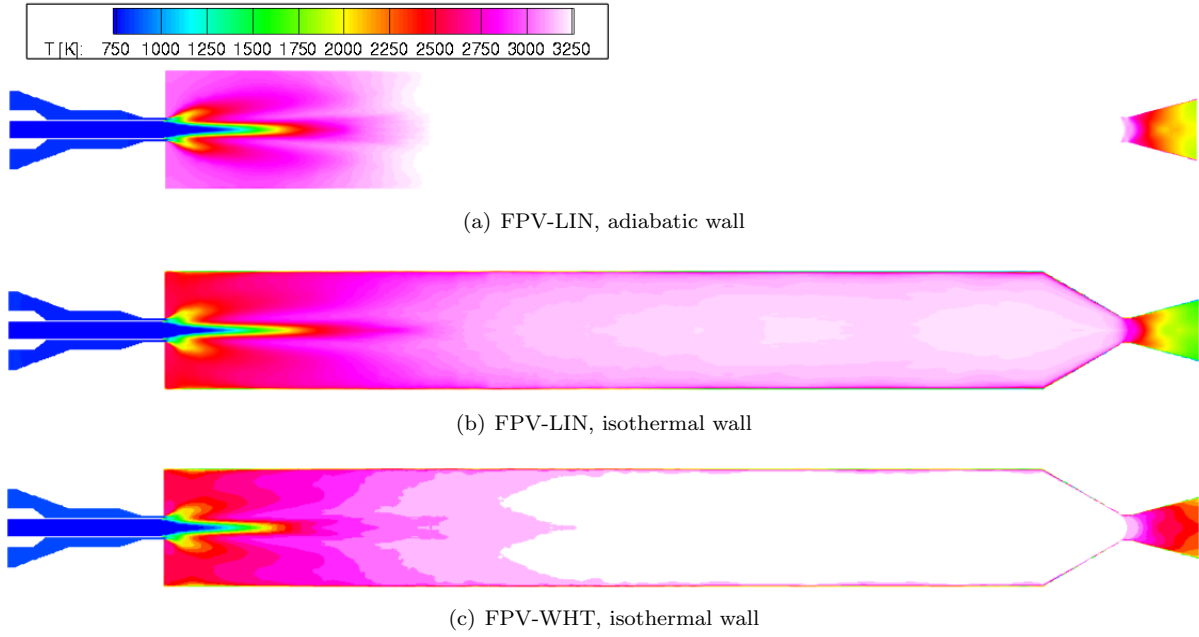


Figure 8. Mean temperature field at the center-plane for (a) FPV-LIN with adiabatic wall, (b) FPV-LIN with isothermal wall, and (c) FPV-WHT with isothermal wall.

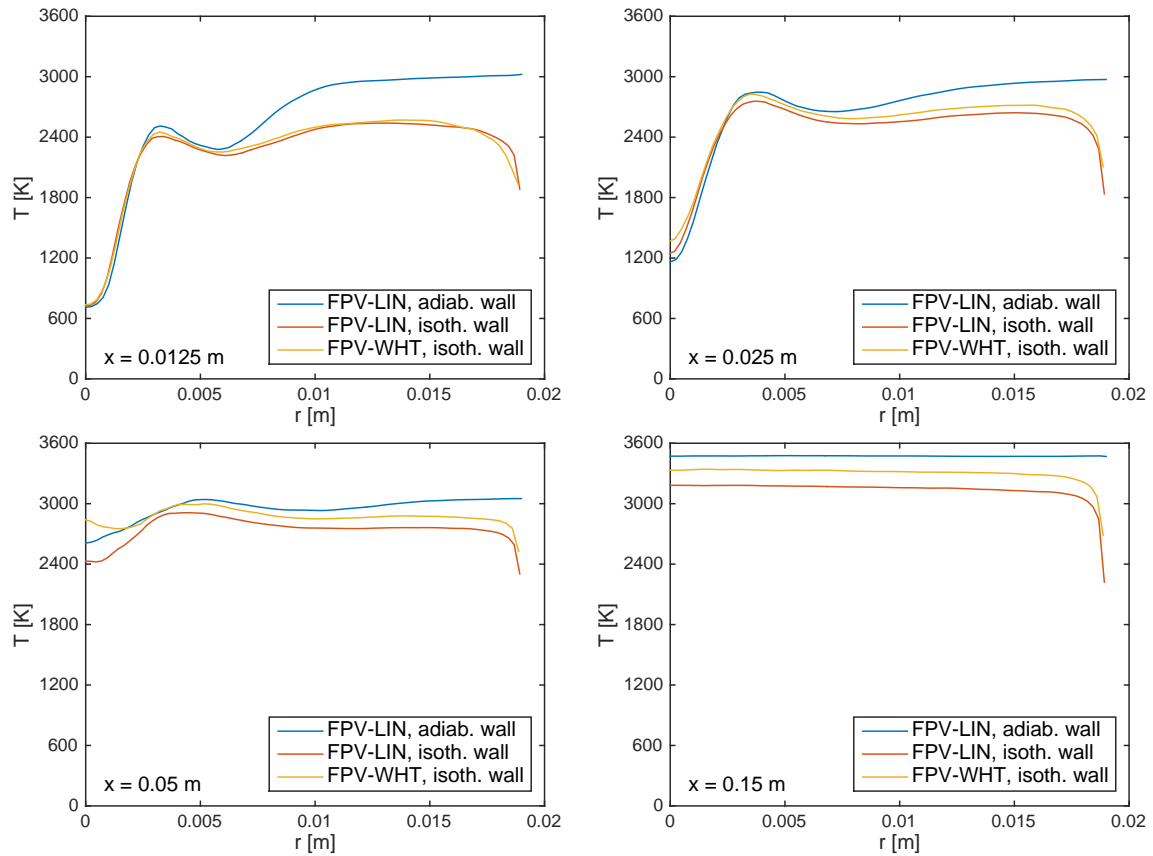


Figure 9. Radial mean temperature profiles predicted for three different cases at axial locations of 0.0125, 0.025, 0.05 and 0.15 m.

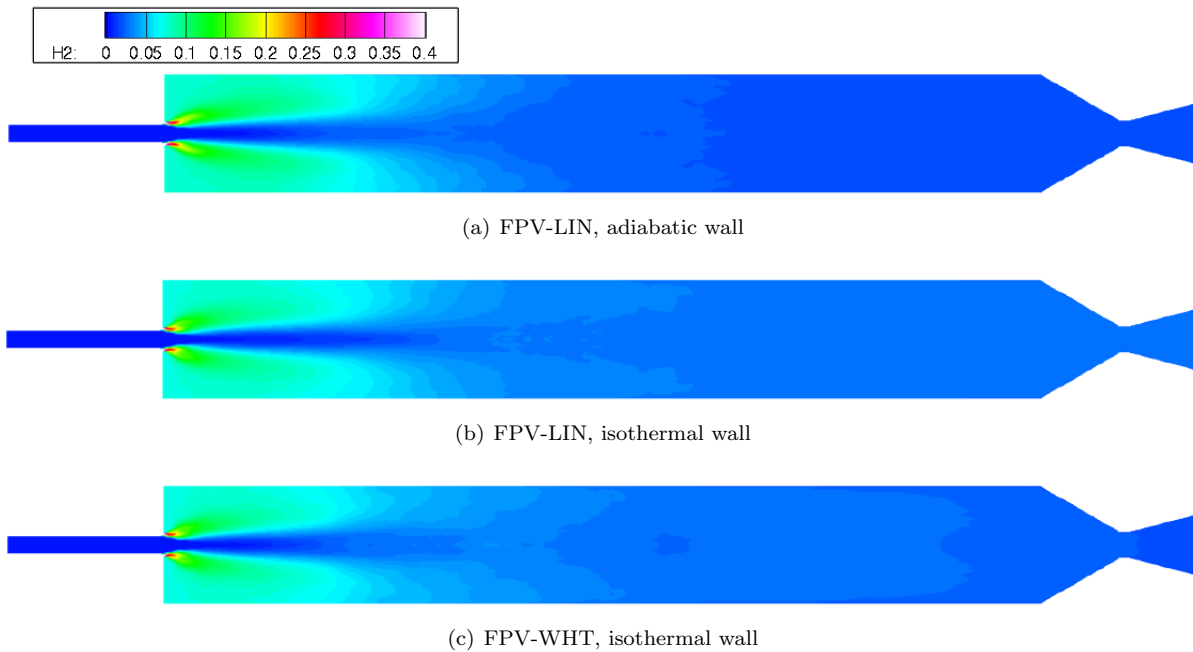


Figure 10. Mean mass fraction field of  $H_2$  at the center-plane for (a) FPV-LIN with adiabatic wall, (b) FPV-LIN with isothermal wall, and (c) FPV-WHT with isothermal wall.

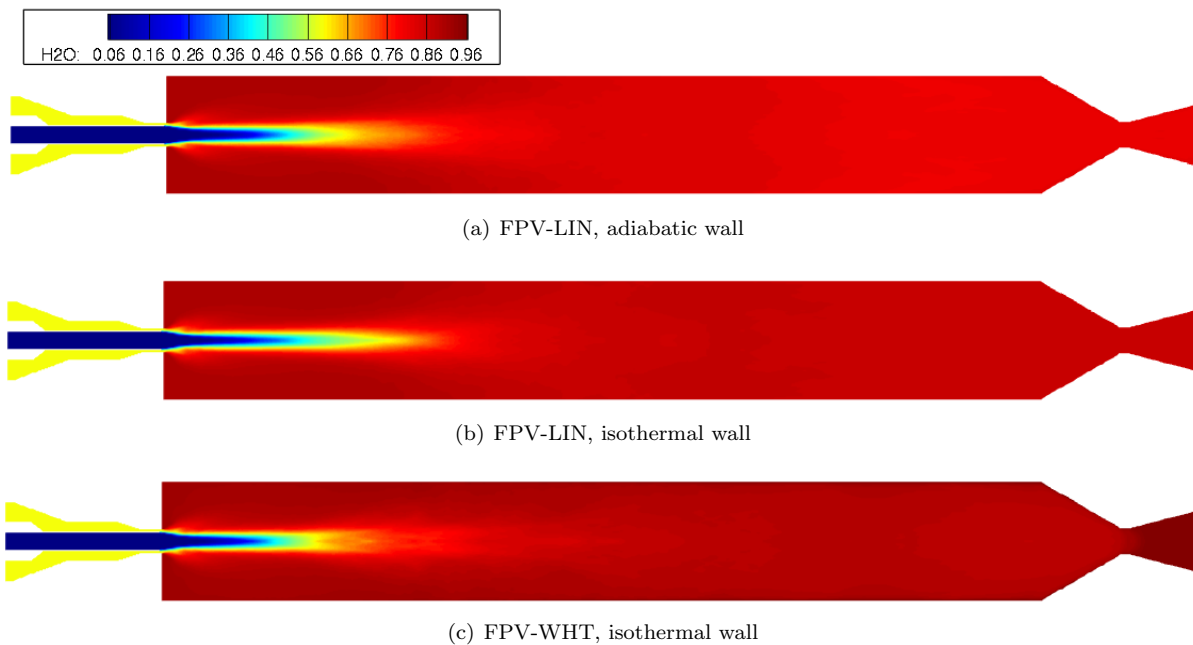


Figure 11. Mean mass fraction field of  $H_2O$  at the center-plane for (a) FPV-LIN with adiabatic wall, (b) FPV-LIN with isothermal wall, and (c) FPV-WHT with isothermal wall.

the two cases with isothermal boundary conditions, the FPV-WHT shows consistently higher temperatures in comparison with the FPV-LIN model.

Figures 10 and 11 shows the mean mass fraction fields of  $H_2$  and  $H_2O$  at the center-plane for the three cases considered. It can be seen from Fig. 10 that the difference in the  $H_2$  mass fraction from the three cases considered is not significant, with the two isothermal cases having slightly lower values of  $H_2$  mass fraction downstream. The three cases show comparable results for the mass fraction of  $O_2$ , and the results

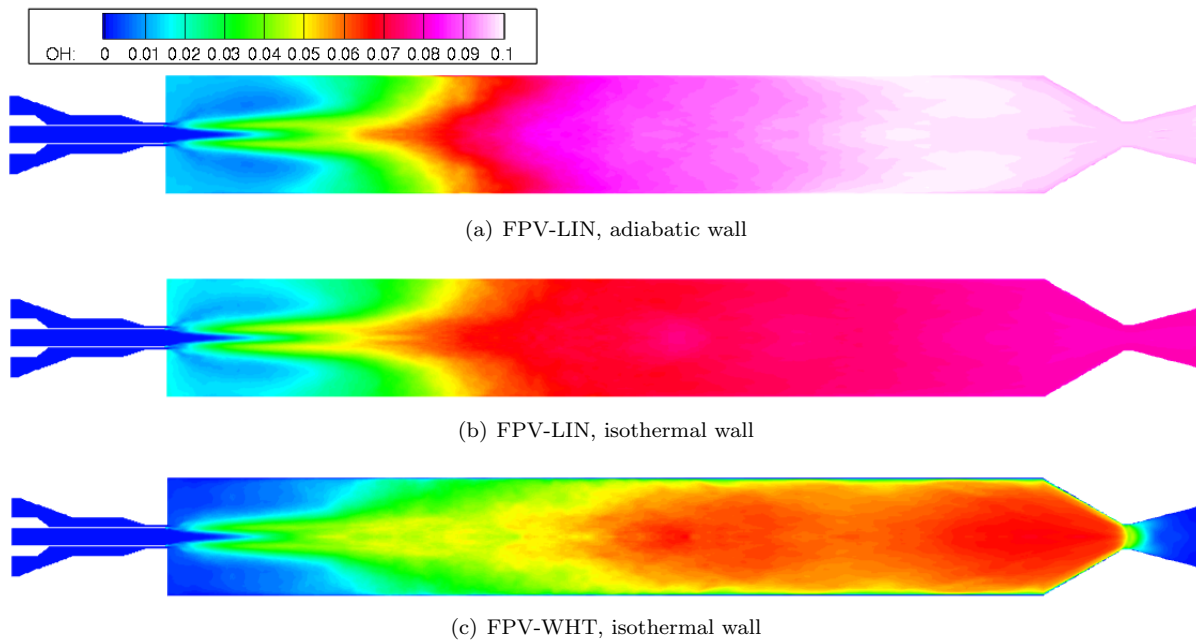


Figure 12. Mean mass fraction field of OH at the center-plane for (a) FPV-LIN with adiabatic wall, (b) FPV-LIN with isothermal wall, and (c) FPV-WHT with isothermal wall.

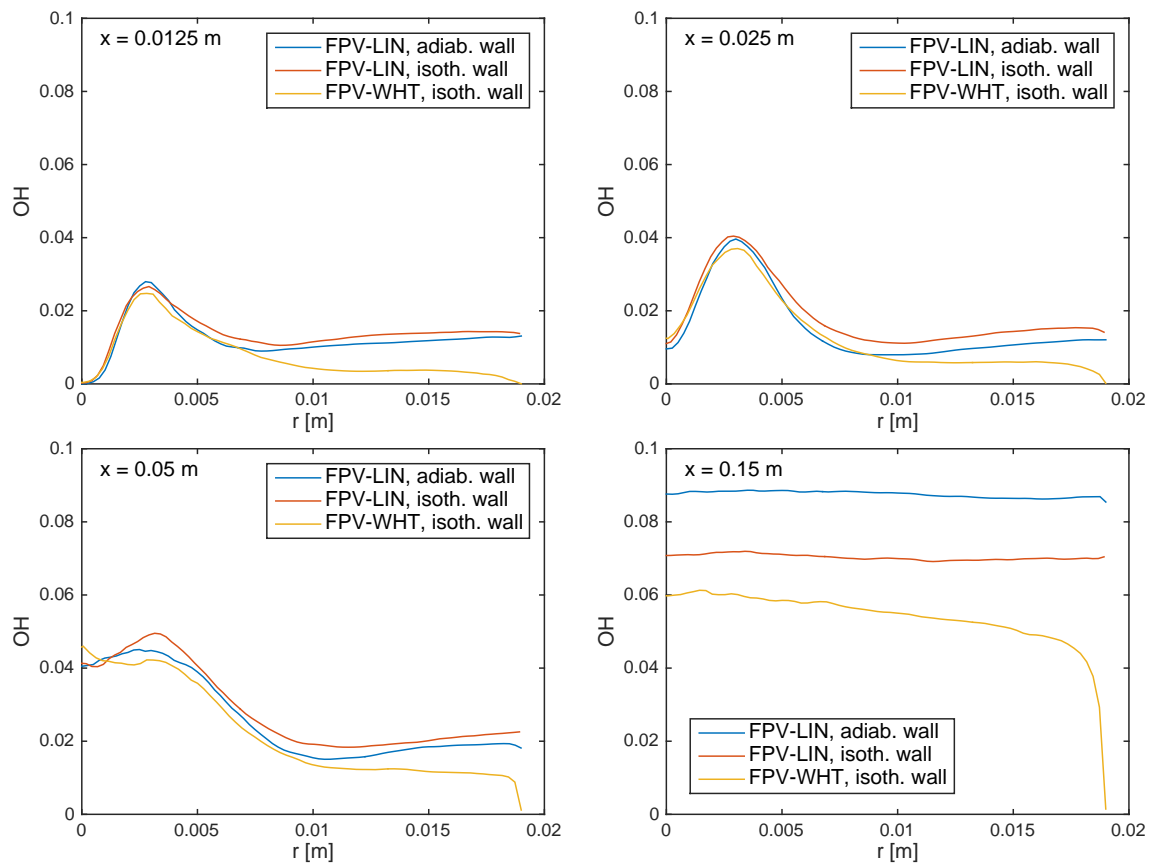


Figure 13. Radial mean OH mass fraction profiles predicted for three different cases at axial locations of 0.0125, 0.025, 0.05 and 0.15 m.

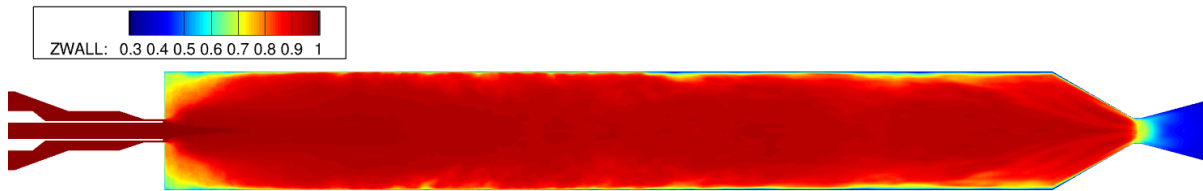


Figure 14. Mean profile of variable  $Z_{\text{wall}}$  at the center-plane for the case with isothermal wall using the FPV-WHT model.

are omitted here. For the mass fraction of  $\text{H}_2\text{O}$  shown in Fig. 11, noticeable difference can be observed downstream the chamber that the FPV-WHT model predicts higher level of the product compared with the FPV-LIN model. This is consistent with the flamelet solution shown in Fig. 2(b) where more  $\text{H}_2\text{O}$  species is generated with increasing heat loss effects.

Results of mean OH mass fraction are presented in Figs. 12 and 13, showing as contours at center-plane and radial profiles at several axial locations. Interestingly, even with a flamelet table generated under adiabatic conditions, the FPV-LIN model with isothermal wall predicts significantly lower OH mass fraction downstream the combustor compared to the case with adiabatic wall boundary conditions. For the regions near the injector, the FPV-LIN model predicts similar levels of OH mass fractions regardless of the wall boundary conditions applied, which can be clearly seen in Fig. 13. For the comparison between the two isothermal cases, FPV-WHT shows significantly lower levels of OH mass fraction compared with the FPV-LIN model in the near-wall regions, emphasizing effects of the wall heat loss on the kinetics. This results are consistent with the flamelet solution as shown in Fig. 2(c) where OH mass fraction is reduced with the presence of wall heat transfer. Since no heat loss effects are taken into account in adiabatic table for the FPV-LIN model, the OH mass fraction profiles show almost zero gradient along the chamber wall. However, for the FPV-WHT model, with the wall heat transfer effect considered, a boundary-layer type profile can clearly be seen in Fig. 12 for the OH mass fraction.

The effects of wall heat transfer can better be explained using Fig. 14 in which the mean profile of variable  $Z_{\text{wall}}$  from the case with FPV-WHT model is plotted at the center-plane. Recall that this variable defines the location where the additional boundary condition in the mixture fraction space is placed, see Section III. The value of  $Z_{\text{wall}}$  is also tabulated in the chemistry table for visualization purposes. As can be seen from Fig. 14, the majority of the region inside the combustion chamber has a  $Z_{\text{wall}}$  value close to unity, meaning that the diffusion flame can be represented by the flamelet calculated under adiabatic conditions. However, for regions near the wall, significant heat loss effects are depicted by the non-unity values of  $Z_{\text{wall}}$ . A large region at the corners of the combustor near the injector shows  $Z_{\text{wall}}$  values significantly deviated from unity. The non-unity region of  $Z_{\text{wall}}$  near the wall downstream the combustor increases with increasing

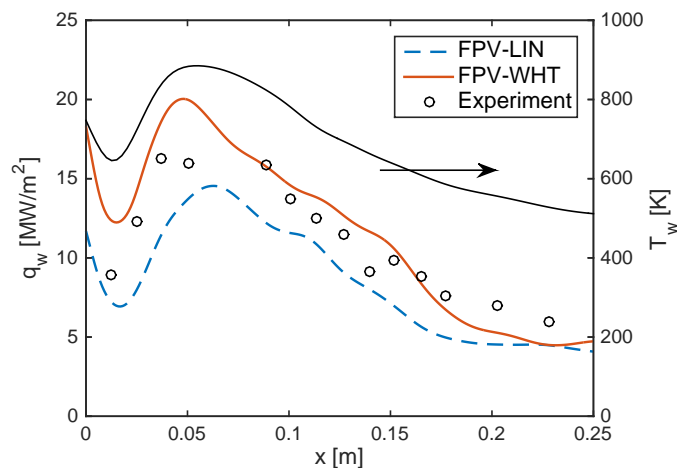


Figure 15. Distribution of heat flux along the chamber wall predicted by different models in comparison with measurements. Temperature profile along the wall is also shown for reference.

axial location.

Finally, the predictions of the wall heat flux using both the FPV-LIN and FPV-WHT models are compared with experimental measurements along the chamber wall, and the results are presented in Fig. 15. The wall temperature profile, which is applied as the isothermal wall boundary conditions is also shown for reference. It can be seen from Fig. 15 that the FPV-LIN model shows underprediction of the wall heat flux for all the measurement stations. The results from the FPV-WHT model show improvement both in the heat flux peak region of  $0.05 \text{ m} < x < 0.1 \text{ m}$ , and downstream of the combustor chamber. However, overpredictions near the injector can be observed in comparison with the measurement at the first measured station. The cause of this discrepancy needs further investigation which is the subject of future work. The effect of heat loss on the reaction process can be further analyzed if the joint statistics of the mass fractions of species and temperature are considered. Such analysis as carried out in<sup>48</sup> is also of interest for future work.

## VI. Conclusions

A turbulent combustion model for the prediction of wall-heat transfer has been developed. This model extends the adiabatic flamelet/progress variable model by introducing a permeable thermal boundary condition into the flamelet equations, and allows for prescribing thermal boundary conditions. This model is self-contained and does not introduce additional constraints on prescribed enthalpy profiles or other parameters. Flame quenching is also naturally incorporated in this formulation.

This flamelet-formulation with wall-heat transfer was incorporated into a flamelet/progress variable approach, and the performance of this model was examined in the context of direct simulation of a turbulent  $\text{H}_2/\text{O}_2$  diffusion flame that is stabilized at an inert isothermal wall. Model predictions for mean-flow quantities and wall-heat flux were compared with DNS-results, and it was shown that this formulation provides an adequate description of convective heat-loss effects.

The model was subsequently applied to a wall-resolved LES of a uni-element rocket injector. Model predictions obtained with the non-adiabatic combustion model show a pronounced effect of wall-heat losses on the temperature and minor species. These effects are not only confined to the near-wall region, but are also evident in the combustor core region and recirculation region, which are characterized by long residence times. The developed model shows improved prediction of the wall heat flux compared to the model utilizing an adiabatic chemistry table.

## Acknowledgments

The authors gratefully acknowledge financial support through NASA with Award No. NNM13AA11G. The resources of the National Energy Research Scientific Computing Center, which is supported by the Office of Science of the U.S. Department of Energy under Contract No. DE-AC02-05CH11231, are acknowledged. Part of the resources supporting this work was provided by the NASA High-End Computing (HEC) Program through the NASA Advanced Supercomputing (NAS) Division at Ames Research Center.

## References

- <sup>1</sup>Dreizler, A. and Böhm, B., “Advanced laser diagnostics for an improved understanding of premixed flame-wall interactions,” *Proc. Combust. Inst.*, Vol. 35, 2015, pp. 37–64.
- <sup>2</sup>*Flight and Aircraft Engineer, Rocket-motor cooling*, April 29th, 1955.
- <sup>3</sup>Goetz, O. K. and Monk, J. C., “Combustion device failures during space shuttle main engine development,” *5th International Symposium on Liquid Space Propulsion Long Life Combustion Devices Technology*, Chattanooga, TN, 2003.
- <sup>4</sup>Riccias, J., Haidn, O. J., and Zametaev, E. B., “Influence of time dependent effects on the estimated life time of liquid rocket combustion chamber walls,” *40th AIAA/ASME/SAE/ASEE Joint Propulsion Conference and Exhibit*, No. 2004-3670, Fort Lauderdale, FL, 2004.
- <sup>5</sup>Oefelein, J. and Yang, V., “Modeling high-pressure mixing and combustion processes in liquid rocket engines,” *J. Prop. Power*, Vol. 14, 1998, pp. 843–857.
- <sup>6</sup>Schmitt, T., Méry, Y., Boileau, M., and Candel, S., “Large-eddy simulation of oxygen/methane flames under transcritical conditions,” *Proc. Combust. Inst.*, Vol. 33, 2011, pp. 1383–1390.
- <sup>7</sup>Guézennec, N., Masquelet, M., and Menon, S., “Large eddy simulation of flame-turbulence interactions in a LOX-CH4 shear coaxial injector,” *50th AIAA Aerospace Sciences Meeting*, No. 2012-1267, Nashville, TN, 2012.
- <sup>8</sup>Garby, R., Selle, L., and Poinot, T., “Large-eddy simulation of combustion instabilities in a variable-length combustor,” *C. R. Mecanique*, Vol. 341, 2013, pp. 220–229.

- <sup>9</sup>Wang, X. and Yang, V., “Supercritical mixing and combustion of liquid-oxygen/kerosene bi-swirl injectors,” *J. Propul. Power*, Vol. 33, No. 2, 2017, pp. 316–322.
- <sup>10</sup>Ma, P. C., Banuti, D., Hickey, J.-P., and Ihme, M., “Numerical framework for transcritical real-fluid reacting flow simulations using the flamelet progress variable approach,” *55th AIAA Aerospace Sciences Meeting*, No. 2017-0143, Orlando, FL, 2017.
- <sup>11</sup>Wu, H., Ma, P. C., Lv, Y., and Ihme, M., “MVP-Workshop contribution: Modeling of Volvo bluff body flame experiment,” *55th AIAA Aerospace Sciences Meeting*, No. 2017-1573, Grapevine, TX, 2017.
- <sup>12</sup>Esclapez, L., Ma, P. C., Mayhew, E., Xu, R., Stouffer, S., Lee, T., Wang, H., and Ihme, M., “Fuel effects on lean blow-out in a realistic gas turbine combustor,” *Combust. Flame*, Vol. 181, 2017, pp. 82–99.
- <sup>13</sup>Park, G. I. and Moin, P., “An improved dynamic non-equilibrium wall-model for large eddy simulation,” *Phys. Fluids*, Vol. 26, No. 1, 2014, pp. 37–48.
- <sup>14</sup>Larsson, J., Kawai, S., Bodart, J., and Bermejo-Moreno, I., “Large eddy simulation with modeled wall-stress: recent progress and future directions,” *Mechanical Engineering Reviews*, Vol. 3, No. 1, 2016, pp. 15–00418.
- <sup>15</sup>Ma, P. C., Ewan, T., Jainski, C., Lu, L., Dreizler, A., Sick, V., and Ihme, M., “Development and analysis of wall models for internal combustion engine simulations using high-speed micro-PIV measurements,” *Flow Turb. Combust.*, Vol. 98, No. 1, 2017, pp. 283–309.
- <sup>16</sup>Ma, P. C., Greene, M., Sick, V., and Ihme, M., “Non-equilibrium wall-modeling for internal combustion engine simulations with wall heat transfer,” *Int. J. Engine Res.*, Vol. 18, No. 1-2, 2017, pp. 15–25.
- <sup>17</sup>Tucker, P. K., Menon, S., Merkle, C. L., Oefelein, J. C., and Yang, V., “Validation of high-fidelity CFD simulations for rocket injector design,” *44th AIAA/ASME/SAE/ASEE Joint Propulsion Conference and Exhibit*, No. 2008-5226, Hartford, CT, 2008.
- <sup>18</sup>Wu, H., See, Y. C., Wang, Q., and Ihme, M., “A Pareto-efficient combustion framework with submodel assignment for predicting complex flame configurations,” *Combust. Flame*, Vol. 162, No. 11, 2015, pp. 4208–4230.
- <sup>19</sup>Wu, H. and Ihme, M., “Compliance of combustion models for turbulent reacting flow simulations,” *Fuel*, Vol. 186, 2016, pp. 853–863.
- <sup>20</sup>Yang, S., Wang, X., Yang, V., Sun, W., and Huo, H., “Comparison of flamelet/progress-variable and finite-rate chemistry LES models in a preconditioning scheme,” *55th AIAA Aerospace Sciences Meeting*, No. 2017-0605, Grapevine, TX, 2017.
- <sup>21</sup>Yang, S., *Effects of detailed finite rate chemistry in turbulent combustion*, Ph.D. thesis, Aerospace Engineering, Georgia Institute of Technology, 2017.
- <sup>22</sup>Bray, K. N. C. and Peters, N., “Laminar flamelets in turbulent flames,” *Turbulent Reacting Flows*, edited by P. A. Libby and F. A. Williams, Academic Press, London, 1994, pp. 63–113.
- <sup>23</sup>Marracino, B. and Lentini, D., “Radiation modelling in non-luminous nonpremixed turbulent flames,” *Combust. Sci. Tech.*, Vol. 128, No. 1-6, 1997, pp. 23–48.
- <sup>24</sup>Hossain, M., Jones, J. C., and Malalasekera, W., “Modelling of a bluff-body nonpremixed flame using a coupled radiation/flamelet combustion model,” *Flow, Turb. Combust.*, Vol. 67, No. 3, 2001, pp. 217–234.
- <sup>25</sup>Fiorina, B., Baron, R., Gicquel, O., Thevenin, D., Carpentier, S., and Darabiha, N., “Modelling non-adiabatic partially premixed flames using flame-prolongation of ILDM,” *Comb. Theory Modelling*, Vol. 7, 2003, pp. 449–470.
- <sup>26</sup>Navarro-Martinez, S., Kronenburg, A., and di Mare, F., “Conditional moment closure for large eddy simulation,” *Flow, Turb. Combust.*, Vol. 75, No. 1-4, 2005, pp. 245–274.
- <sup>27</sup>Shunn, L., *Large-eddy simulation of combustion systems with convective heat-loss*, Ph.D. thesis, Stanford University, 2009.
- <sup>28</sup>Cecere, D., Giacomazzi, E., Picchia, F., Arcidiacono, N., Donato, F., and Verzicco, R., “A non-adiabatic flamelet progress-variable approach for LES of turbulent premixed flames,” *Flow, Turb. Combust.*, Vol. 86, No. 3-4, 2011, pp. 667–688.
- <sup>29</sup>Ketelheun, A., Kuenne, G., and Janicka, J., “Heat transfer modeling in the context of large eddy simulation of premixed combustion with tabulated chemistry,” *Flow, Turb. Combust.*, Vol. 91, No. 4, 2013, pp. 867–893.
- <sup>30</sup>Proch, F. and Kempf, A. M., “Modeling heat loss effects in the large eddy simulation of a model gas turbine combustor with premixed flamelet generated manifolds,” *Proc. Combust. Inst.*, Vol. 35, 2015, pp. 3337–3345.
- <sup>31</sup>Gottlieb, S., Shu, C.-W., and Tadmor, E., “Strong stability-preserving high-order time discretization methods,” *SIAM Rev.*, Vol. 43, No. 1, 2001, pp. 89–112.
- <sup>32</sup>Khalighi, Y., Nichols, J. W., Lele, S., Ham, F., and Moin, P., “Unstructured large eddy simulation for prediction of noise issued from turbulent jets in various configurations,” *17th AIAA/CEAS Aeroacoustics Conference*, No. 2011-2886, Portland, OR, 2011.
- <sup>33</sup>Hickey, J.-P., Ma, P. C., Ihme, M., and Thakur, S., “Large eddy simulation of shear coaxial rocket injector: Real fluid effects,” *49th AIAA/ASME/SAE/ASEE Joint Propulsion Conference*, No. 2013-4071, San Jose, CA, 2013.
- <sup>34</sup>Ma, P. C., Lv, Y., and Ihme, M., “An entropy-stable hybrid scheme for simulations of transcritical real-fluid flows,” *J. Comput. Phys.*, Vol. 340, 2017, pp. 330–357.
- <sup>35</sup>Peters, N., “Laminar diffusion flamelet models in non-premixed turbulent combustion,” *Prog. Energy Combust. Sci.*, Vol. 10, No. 3, 1984, pp. 319–339.
- <sup>36</sup>Vervisch, L. and Poinso, T., “Direct numerical simulation of non-premixed turbulent flames,” *Annu. Rev. Fluid Mech.*, Vol. 30, 1998, pp. 655–691.
- <sup>37</sup>Lee, D. J., Thakur, S., Wright, J., Ihme, M., and Shyy, W., “Characterization of flow field structure and species composition in a shear coaxial rocket GH<sub>2</sub>/GO<sub>2</sub> injector: Modeling of wall heat losses,” *47th AIAA/ASME/SAE/ASEE Joint Propulsion Conference and Exhibit*, No. 2011-6125, San Diego, CA, 2011.
- <sup>38</sup>Pitsch, H., “FLAMEMASTER v3.3.10: A C++ computer program for 0D combustion and 1D laminar flame calculations,” 1998.
- <sup>39</sup>Saghafian, A., Terrapon, V. E., and Pitsch, H., “An efficient flamelet-based combustion model for compressible flows,” *Combust. Flame*, Vol. 162, No. 3, 2015, pp. 652–667.

- <sup>40</sup>Pal, S., Marshall, W., Woodward, R., and Santoro, R., “Wall heat flux measurements for a uni-element GO<sub>2</sub>/GH<sub>2</sub> shear coaxial injector,” 2006, Third International Workshop on Rocket Combustion Modeling, Paris, France, March, 13-15.
- <sup>41</sup>Wu, H. and Ihme, M., “Modeling of wall heat transfer and flame/wall interaction: A flamelet model with heat-loss effects,” *9th U. S. National Combustion Meeting*, Cincinnati, OH, 2015.
- <sup>42</sup>Wang, Y. and Trouvé, A., “Direct numerical simulation of nonpremixed flame-wall interactions,” *Combust. Flame*, Vol. 144, 2006, pp. 461–475.
- <sup>43</sup>Pope, S. B., *Turbulent Flows*, Cambridge University Press, Cambridge, 2000.
- <sup>44</sup>Klein, M., Sadiki, A., and Janicka, J., “A digital filter based generation of inflow data for spatially developing direct numerical or large eddy simulations,” *J. Comp. Phys.*, Vol. 186, No. 2, 2003, pp. 652–665.
- <sup>45</sup>Marinov, N. M., Westbrook, C. K., and Pitz, W. J., “Detailed and global chemical kinetics model for hydrogen,” *Transport Phenomena in Combustion*, edited by S. H. Chen, Vol. 1, Taylor & Francis, Washington, DC, 1996, pp. 118–129.
- <sup>46</sup>Vreman, A., “An eddy-viscosity subgrid-scale model for turbulent shear flow: Algebraic theory and applications,” *Phys. Fluids.*, Vol. 16, No. 10, 2004, pp. 3670–3681.
- <sup>47</sup>Burke, M. P., Chaos, M., Ju, Y., Dryer, F. L., and Klippenstein, S. J., “Comprehensive H<sub>2</sub>/O<sub>2</sub> kinetic model for high-pressure combustion,” *Int. J. Chem. Kinet.*, Vol. 44, No. 7, 2012, pp. 444–474.
- <sup>48</sup>Johnson, R., Wu, H., and Ihme, M., “A general probabilistic approach for the quantitative assessment of LES combustion models,” *Combust. Flame*, Vol. 183, 2017, pp. 88–101.